Neuron, Volume *108*

Supplemental Information

Behavioral and Neural Bases of Tactile Shape Discrimination Learning in Head-Fixed Mice

Jinho Kim, Andrew Erskine, Jonathan Andrew Cheung, and Samuel Andrew Hires

Supplementary Figure 1 (related to Figure 1)

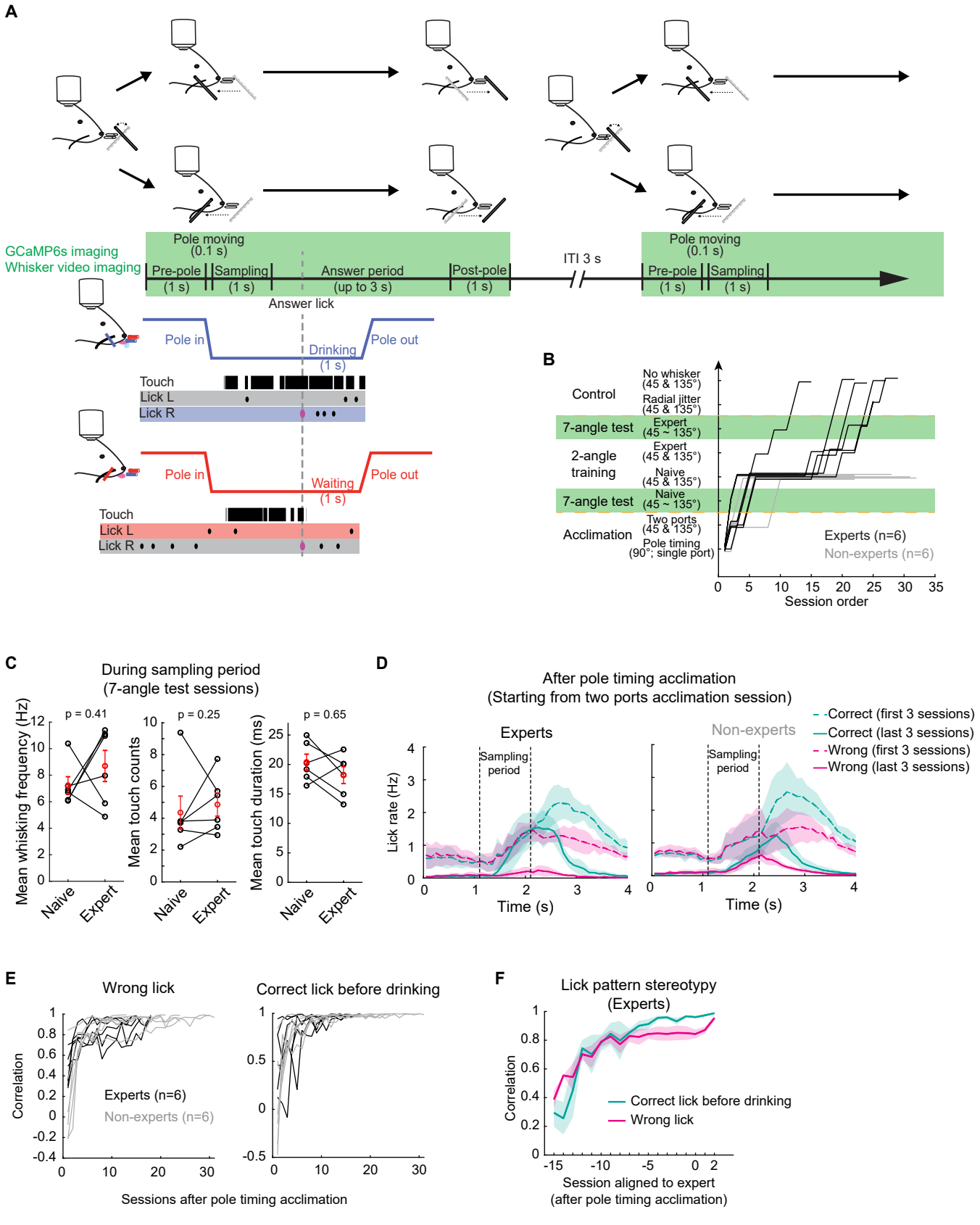

Figure S1 (related to Figure 1). Trial and training structure, and the operant aspect of training.

(A) Task and recording scheme in each trial. A pole was rotated and set to an angle before being presented from the front to the right side of mice. Mice had 1 s of sampling period after object presentation. There was no consequence to licking during this sampling period. First lick within the following 3 s of answer period was recorded as the 'answer lick' (magenta oval), and the object stayed in after the 'answer lick' for 1 s regardless of the outcome. Inter-trial-interval (ITI) was 3 s. Both two-photon GCaMP6s imaging and whisker video imaging (green background) was on hold during this period. The laser for two-photon imaging was blocked during this interval.

(B) Training structure. Mice were trained in a step-wise manner. We analyzed neuronal activities in 7-angle sessions before and after learning (green background). Two mice skipped 'two ports' sessions, and one mouse was lost before the 'no whisker' test at the end.

(C) Three graphs comparing mean whisking frequency (left), mean touch counts (middle), and mean touch duration (right) between naive and expert 7-angle test sessions during sampling period. Black: individual mouse. Red: Mean ± SEM.

(D) Averaged correct lick rates during correct trials (green) and wrong lick rates during wrong trials (magenta) at the beginning of training (first 3 sessions, dotted lines) and at the end of training (last 3 sessions of 2-angle training; solid lines). Those of experts are shown on the left, and those of non-experts on the right. Mean ± SEM.

(E) Correlation of averaged lick patterns from each session to the template. The template was defined by the grand average of last 3 sessions of 2-angle training. For correct lick, we considered lick patterns before drinking only.

(F) Averaged lick pattern correlation to the template (from (E)) in learned mice (n = 6), plotted against sessions counted backwards from the first session of becoming expert. Mean ± SEM.

Supplementary Figure 2 (related to Figure 2)

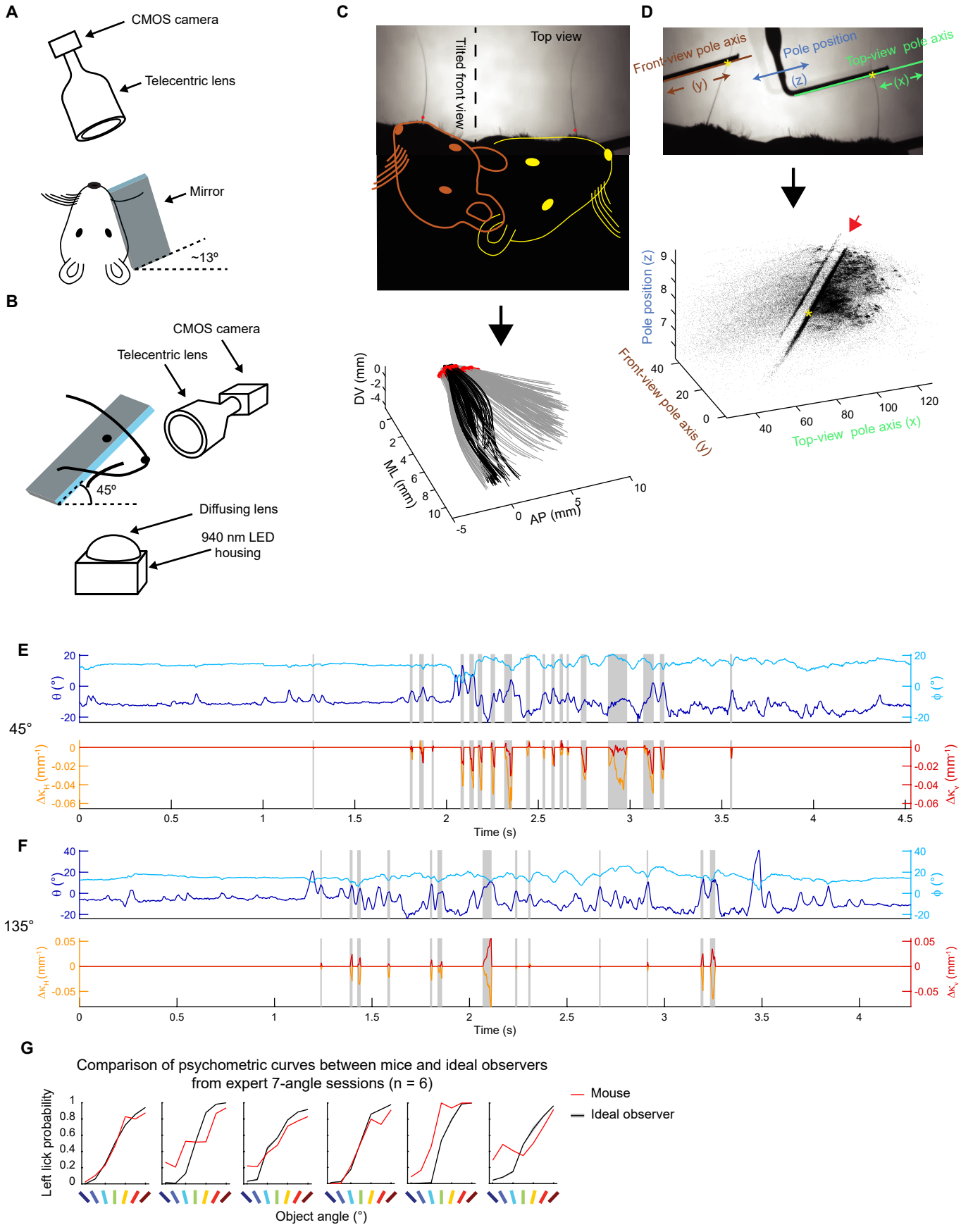

Figure S2 (related to Figure 2). Three-dimensional reconstruction of whisker shape, calculation of whisker-object interaction, and psychometric curves of ideal observers.

(A) A schematic of whisker video recording setup, using a single mirror. Top-down view.

(B) Same as in (A), from the side view.

(C) An example frame of dual view whisker video imaging and its interpretation of each view (top), and frame-by-frame 3-dimensional reconstruction of whisker shape (bottom). Red dots: whisker base points (**STAR Methods**, *Whisker video recording and tracking*). Black: whisker shapes during object touch. Gray: during free whisking. DV: dorsoventral. AP: anteroposterior. ML: mediolateral. Zero values were defined from averaged whisker base points of the trial.

(D) How to detect touch frames. An example video frame during touch and 3 axes annotation (top), and resulting 3D scatter plot (bottom). Yellow asterisk represents whisker-object intersection point in the video images. Top-view value (x) was calculated from the right margin of the image, while front-view value (y) was calculated from the left margin. Resulting 3D scatter plot from all frames of the trials with the same object angle (45° in this example) in a session showed an empty space (red arrow), which represents physical barrier from the object. Points adjacent to this space represent candidate touch frames (**STAR Methods**, *Touch frame detection*). X and y values are in pixels, and z values are in mm.

(E) An example trace of azimuthal angle (θ; blue), elevation angle (φ; cyan), horizontal bending ($\Delta\kappa_H$; orange), and vertical bending ($\Delta\kappa_V$; red) from an example 45° trial. Gray background shows touch frames.

(F) Same as in (E) but from an example 135° trial. Note the different directions of $\Delta\kappa_V$ between (45°; E) and (135°; F).

(G) Psychometric curves of each expert mouse in expert 7-angle sessions (red), compared with the virtual psychometric curves of object-angle decoding model as an ideal observer (black). Gray background represents error bars (SEM) from 10 iterations.

Supplementary Figure 3 (related to Figure 3)

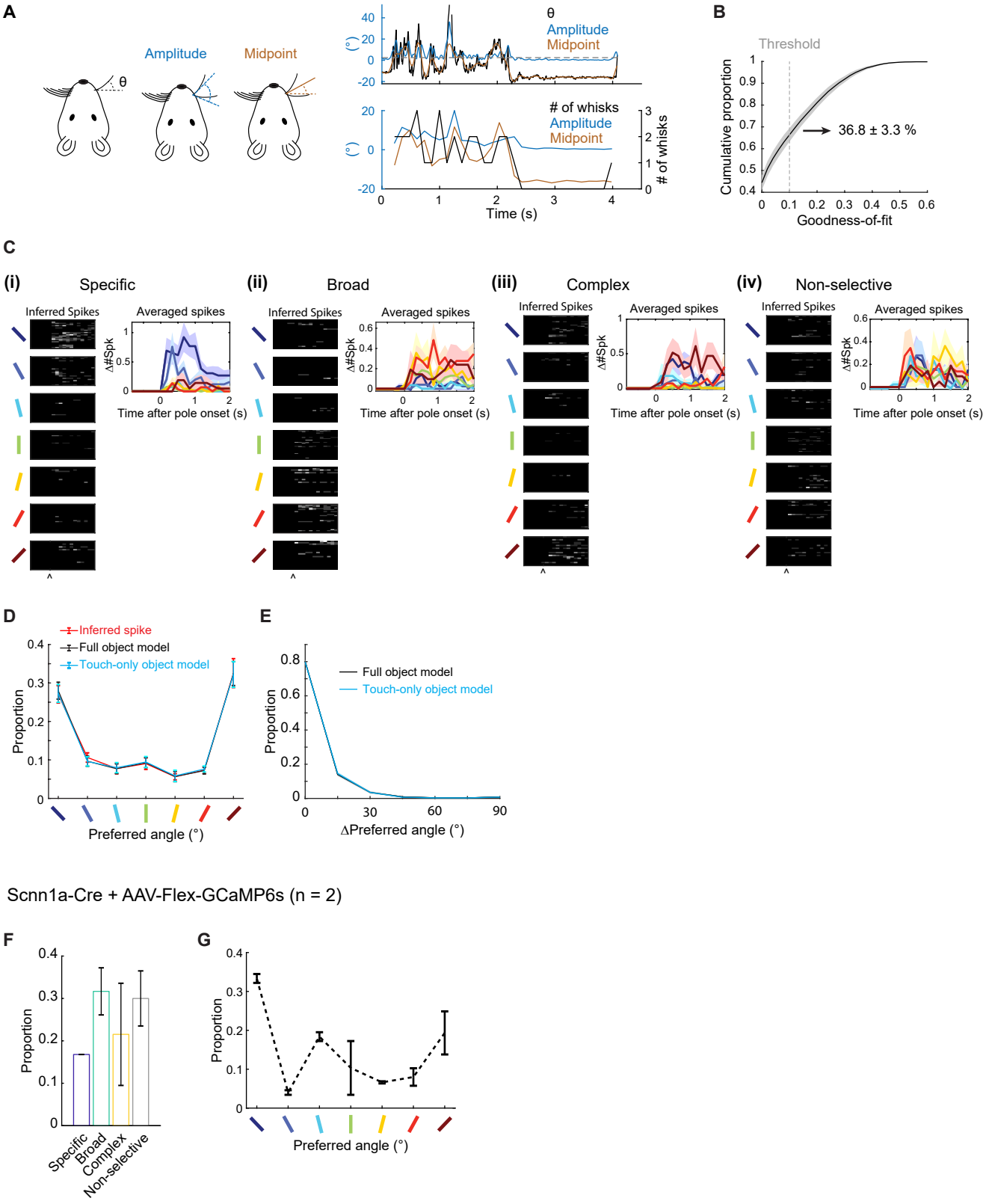

Figure S3 (related to Figure 3). Object-angle tuning in S1.

(A) Schematic for calculating θ, amplitude, and midpoint that describe whisking motion. Graphs on the right show each feature in whisker video imaging (top) and those down-sampled for matching with two-photon imaging (bottom).

(B) Distribution of goodness-of-fit of 'object model' from all naive mice. Vertical dashed gray line indicates the well fit threshold. On average, from naive 7-angle test sessions of 12 mice, 37 % of active neurons exceeded this threshold.

(C) Heat maps of inferred spikes (left) and graphs of averaged spikes (right) grouped by object angles for examples in **Figure 3C**. (i) A specific-tuned neuron, (ii) a broad-tuned neuron, (iii) a complex-tuned neuron, (iv) and a non-selective touch-responsive neuron.

(D) Distribution of preferred angle within angle-tuned neurons, when calculated from inferred spikes (red), full object models (black), and touch-only object models (cyan).

(E) Distribution of preferred angle differences between inferred spikes and full object model (black) or touch-only object model (cyan).

(F) Proportion of each angle tuning type (including non-selective touch-responsive neurons) among touch-responsive neurons in mice that expressed GCaMP6s only in L4 excitatory neurons (Scnn1a-Cre + AAV-Flex-GCaMP6s).

(G) Distribution of preferred object angles in angle-tuned L4 excitatory neurons from these mice.

Data are shown in mean ± SEM.

Supplementary Figure 4 (related to Figure 4)

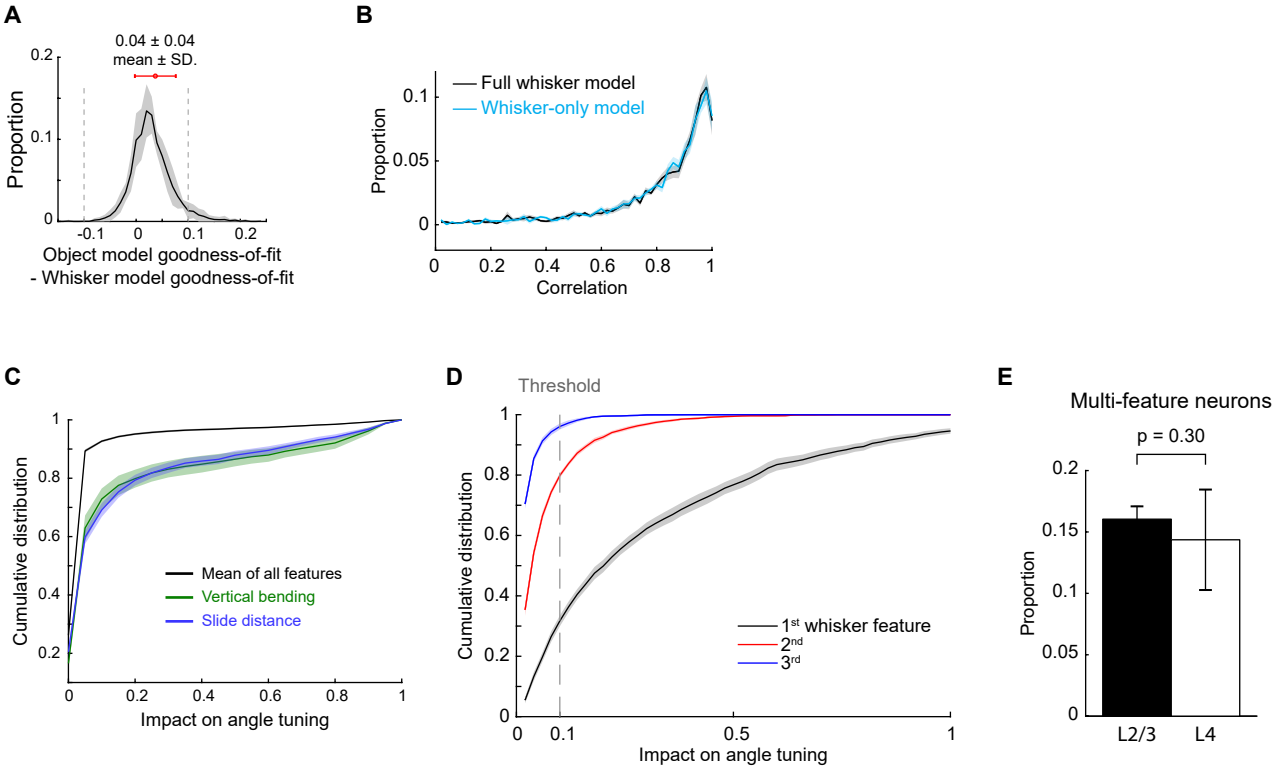

Figure S4 (related to Figure 4). Whisker features that explain object angle tuning in S1 of naive 7-angle test sessions (n = 12).

(A) Distribution of the difference between 'object model' goodness-of-fit (GOF) and 'whisker model' GOF in touch-responsive neurons.

(B) Distribution of correlation between angle tuning curves of inferred spikes and those of full whisker model (black) or whisker-only model (cyan).

(C) Cumulative distribution of averaged impact from all 12 whisker features on angle tuning (black), impact on angle tuning of vertical bending (green), and that of slide distance (blue).

(D) Cumulative distribution of impact on angle tuning from the most impactful feature (1st whisker feature; black), the second-most impactful feature (2nd whisker feature; red), and the third-most impactful feature (3rd whisker feature; blue). Vertical dotted gray line indicates the threshold for defining impactful whisker features on angle tuning in each neuron.

(E) Proportion of L2/3 or L4 active excitatory neurons that had more than 1 impactful whisker feature on angle tuning.

Data are shown in mean ± SEM.

Supplementary Figure 5 (related to Figure 5)

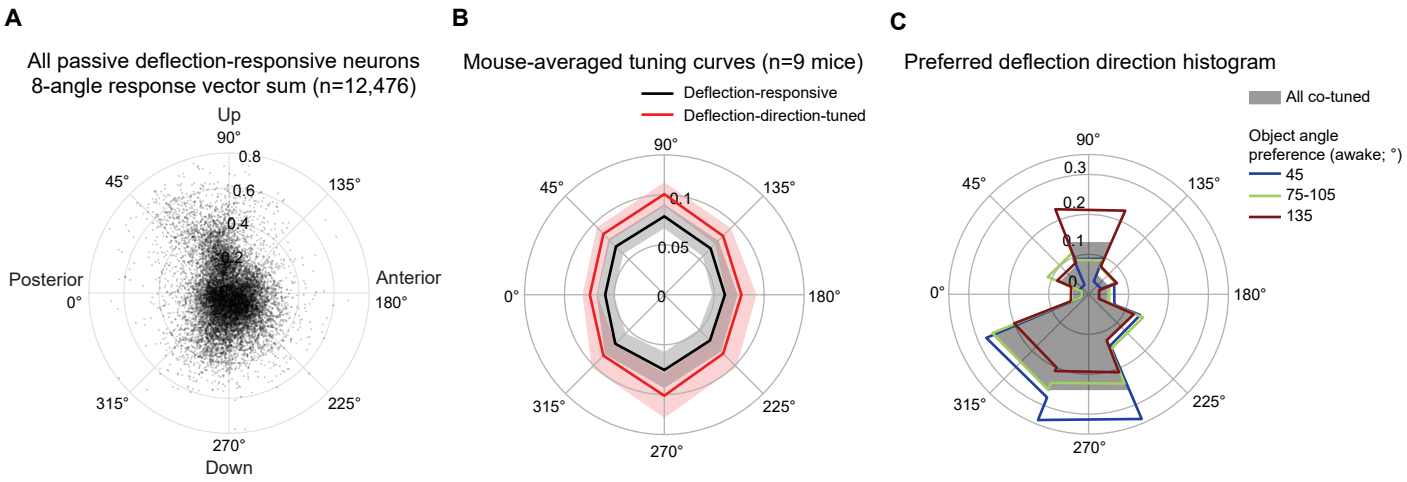

Figure S5 (related to Figure 5). Responses to passive whisker deflection under light isoflurane anesthesia.

(A) A polar plot of the vector sum of mean responses ($\Delta F/F_0$) to 8 deflection directions for all passive deflection-responsive neurons. Each dot represents a neuron (n = 12,476).

(B) Averaged passive whisker deflection response tuning curves from all deflection-responsive neurons (black) and deflection-direction-tuned neurons (red) in 9 mice. $P < 0.05$ from paired t test between mean response to vertical directions (90 and 270°) and horizontal directions (0 and 180°). Mean ± SEM.

(C) Histograms of preferred whisker deflection directions in all co-tuned neurons (gray), neurons preferring 45° (blue), intermediate angles (75-105°; green), and 135° (red) objects in awake naive 7-angle test sessions.

Supplementary Figure 6 (related to Figure 6 and Methods)

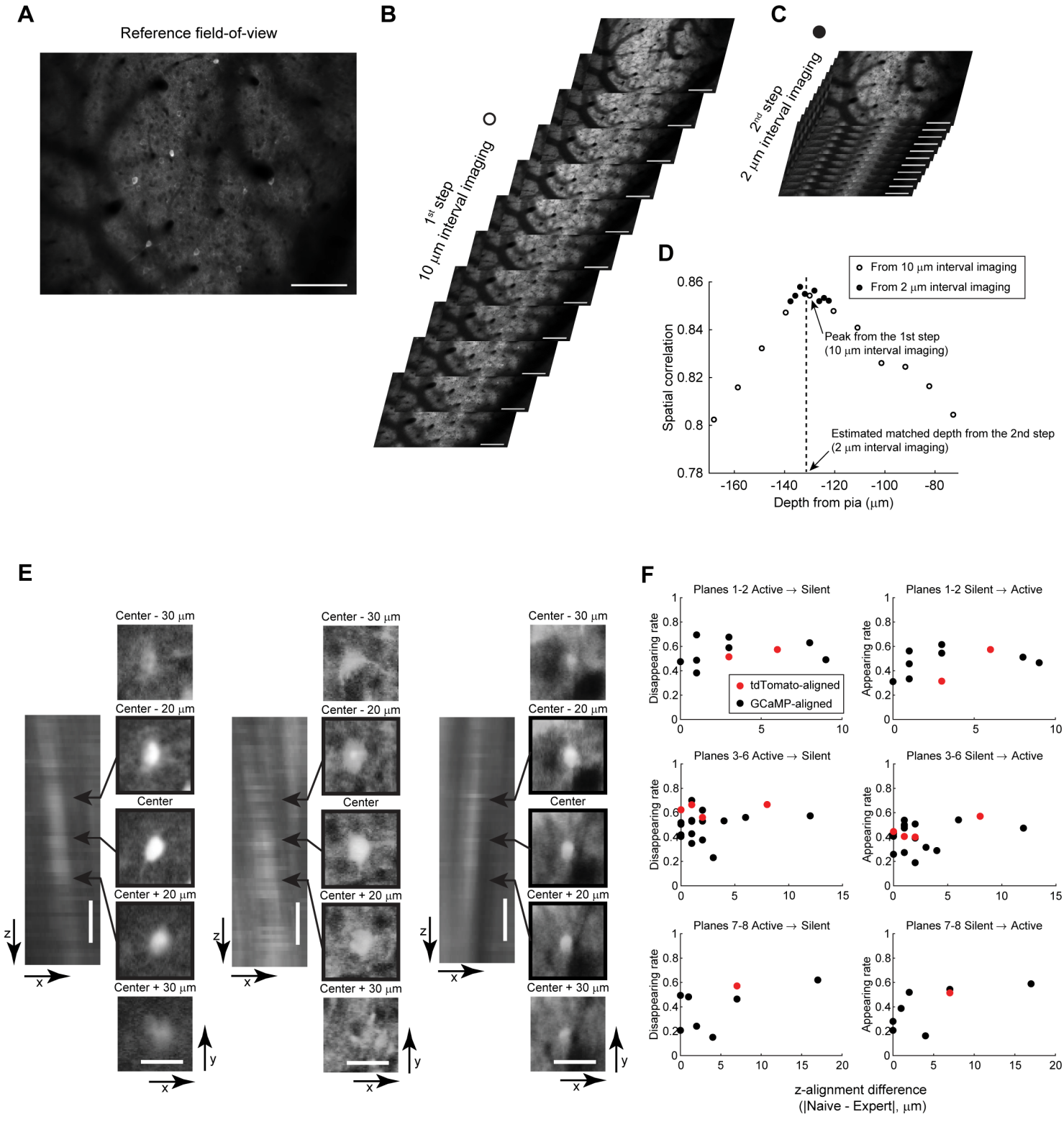

Figure S6 (related to Figure 6 and STAR Methods, *Matching planes across sessions*). Matching imaging planes across sessions.

(A) An example reference field-of-view (FOV). Scale bar, 100 μm.

(B) First step of matching imaging planes by 10 μm interval imaging around approximated position and depth. Spatial correlation values between each of these images and the reference FOV in (A) were calculated after intensity-based spatial registration.

(C) Second step by 2 μm interval imaging around the depth where spatial correlation was the highest between reference FOV and 1st step (B).

(D) Example plot of spatial correlation between the reference FOV and 1st step images (B, open circles) or 2nd step images (C, filled circles). The vertical dotted line indicates the final estimated matched depth after the 2nd step.

(E) X-z averaged images (left) and x-y averaged images (right) from 3 rare cases of nucleus-filled chronically fluorescent neurons from z-stack imaging. X-z images are averaged within the field defined by x-y images. Five x-y images are shown for each neuron, at the depth of -30, -20, 0, 20, and 30 μm from the central depth of the neuron. Scale bars, 20 μm.

(F) Plots of disappearing rate (active → silent; left) or appearing rate (silent → active; right) against z-alignment differences after grouping by upper planes (planes 1-2), middle planes (planes 3-6), and lower planes (planes 7-8). Red: from a tdTomato-expressing mouse. Black, from GCaMP6s-only mice (n = 5).

Supplemenatry Figure 7 (related to Figures 6 and 7)

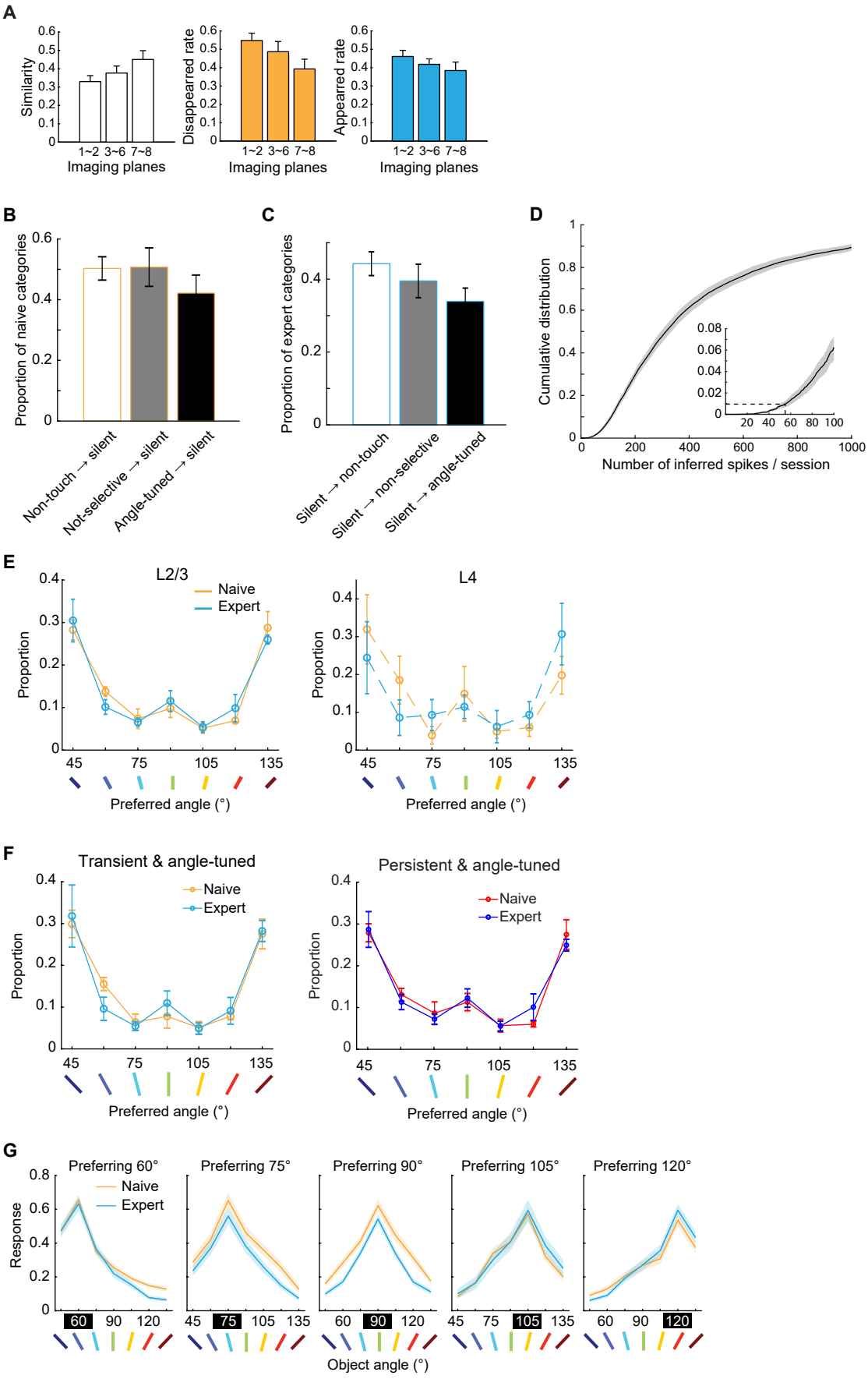

Figure S7 (related to Figures 6 and 7). Active ensemble changes, stable distribution of preferred angles, and averaged angle-tuned responses.

(A) Similarity, disappeared rate, and appeared rate in different imaging planes.

(B) Proportion of naive neurons in each category that fell silent after learning.

(C) Proportion of expert neurons in each category that were silent before learning.

(D) Cumulative distribution of number of inferred spikes from all active neurons within each session, from all 12 sessions (6 naive and 6 expert 7-angle test sessions). Inset, magnified view of 0-100 inferred spikes / session.

(E) Distribution of preferred object angles across training (orange, naive; cyan, expert) in L2/3 (left) and L4 (right).

(F) Distribution of preferred object angles across training within transient & angle-tuned neurons (left) and persistent & angle-tuned neurons (right).

(G) Averaged responses across all neurons that were preferring each object angles from 60 to 120°.

Data are shown in mean ± SEM.

Supplementary Figure 8 (related to Figure 8)

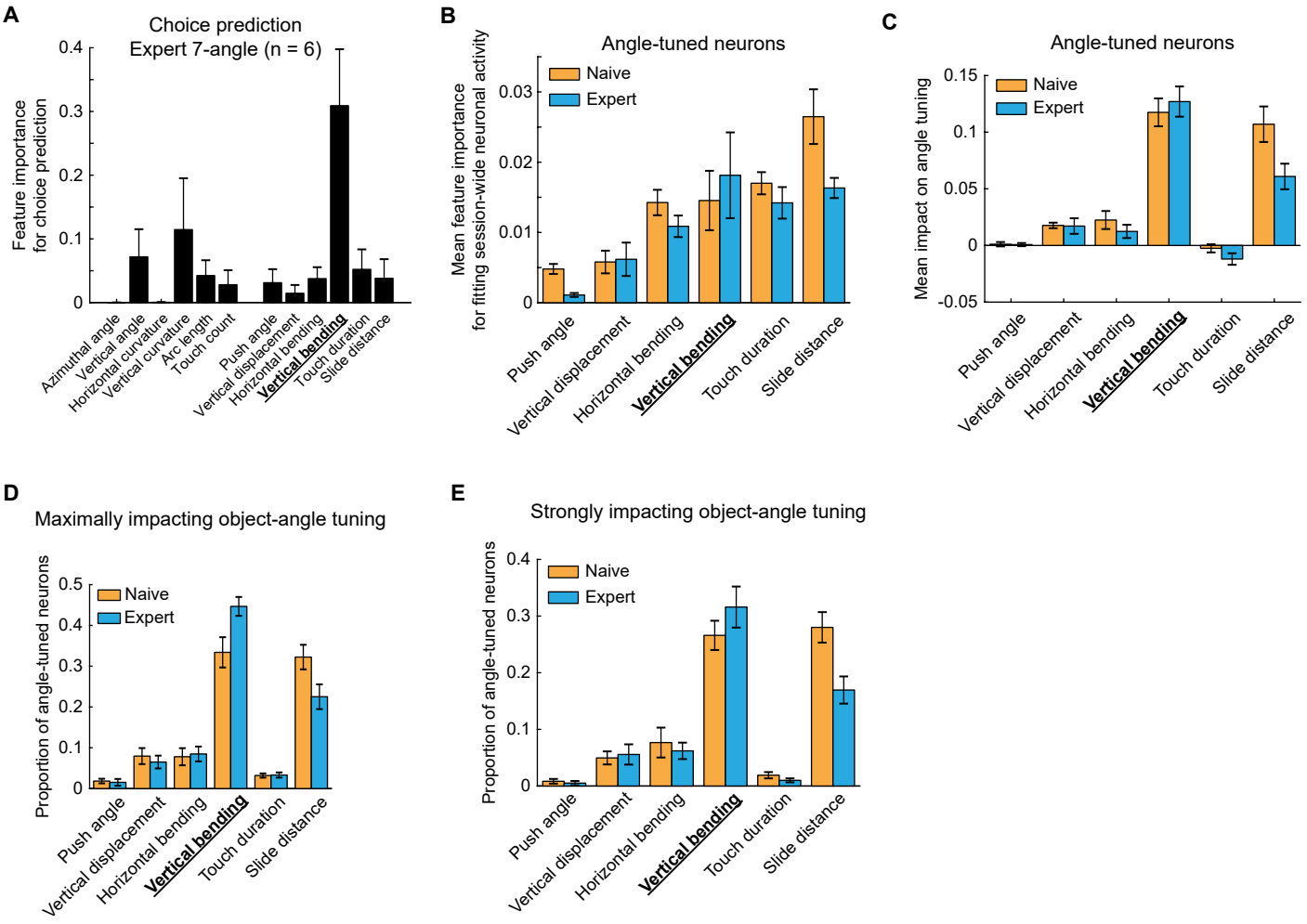

Figure S8 (related to Figure 8). Whisker features in choice prediction, fitting neuronal activities, and impact on angle tuning across object-angle discrimination training.

(A) Bar graphs of mean feature importance on choice prediction for 12 whisker features from expert 7-angle test sessions. The most important feature, vertical bending, is highlighted.

(B) Mouse-averaged feature importance on fitting session-wide neuronal activity in angle-tuned neurons, compared between naive (orange) and expert (cyan) 7-angle test sessions (n = 6 mice).

(C) Mouse-averaged impact on angle tuning in angle-tuned neurons (n = 6 mice).

(D) Proportion of angle-tuned neurons that had each whisker feature during touch as the maximally impacting object-angle tuning (n = 6 mice).

(E) Same as in (D), but for neurons that had strong impacts on object-angle tuning (impact on angle tuning >0.1).

Only whisker features during touch are shown, in mean ± SEM.